Applied Thermal Engineering 221 (2023) 119827

Contents lists available at ScienceDirect

Applied Thermal Engineering

journal homepage: www.elsevier.com/locate/apthermeng

Research Paper

Significant optimization of active thermomagnetic generator for low-grade waste heat recovery

Xianliang Liu [a], Hu Zhang [a,*], Haodong Chen [a], Zhihui Ma [a], Kaiming Qiao [a], Longlong Xie [a], Zhiqiang Ou [b], Jing Wang [c,d,e], Fengxia Hu [c,d,f], Baogen Shen [c,d,g]

[a] School of Materials Science and Engineering, University of Science and Technology Beijing, Beijing 100083, PR China
[b] Inner Mongolia Key Laboratory for Physics and Chemistry of Functional Materials, Inner Mongolia Normal University, Hohhot 010022, PR China
[c] Beijing National Laboratory for Condensed Matter Physics, Institute of Physics, Chinese Academy of Sciences, Beijing 100190, PR China
[d] School of Physical Sciences, University of Chinese Academy of Sciences, Beijing 100049, PR China
[e] Fujian Innovation Academy, Chinese Academy of Sciences, Fuzhou, Fujian 350108, PR China
[f] Songshan Lake Materials Laboratory, Dongguan, Guangdong 523808, PR China
[g] Ningbo Institute of Materials Technology & Engineering, Chinese Academy of Sciences, Ningbo, Zhejiang 315201, PR China

ARTICLE INFO

Keywords:
Thermomagnetic generator
Waste heat recovery
Thermomagnetic effect
Energy conversion

ABSTRACT

Recently, thermomagnetic generator (TMG) based on the thermomagnetic effect is becoming a promising technology for low-grade waste heat recovery. However, poor performance still hinders the application of this novel technology. The performance of TMG is significantly affected by the key device parameters and material properties. Unfortunately, there is a lack of systematic research in this regard. In present work, for the first time, we systematically study the effects of different key device and material parameters on the TMG performance through a combination of experiment and finite element simulation. It demonstrates that the TMG performance is influenced largely by both device and material parameters, especially the cabin size and specific heat capacity. Furthermore, the key device parameters are optimized, i.e., the sample cabin size is shortened from 145 mm to 20 mm, the system temperature range is expanded from 288 ~ 353 K to 276 ~ 361 K, and the cycle period is reduced from 60 s to 10 s. In comparison with the non-optimized experimental peak I of 28.8 μA, the simulated peak I increases largely to 136.1 μA after the optimization. In addition, more I peaks are obtained by shortening the cycle period. The maximum power density P_d and average P_d are 3.6 mW/m^3 K and 0.4 mW/m^3 K, respectively, which are one order of magnitude higher than the values before optimization (0.16 mW/m^3 K and 0.01 mW/m^3 K), and even three orders of magnitude higher than those of other reported TMGs.

1. Introduction

With the rapid development of population and economy, energy demand is also increasing largely. The energy crisis has gradually become a global problem, which has prompted us to develop clean energy and renewable energy. Waste heat from industries, transportation, residents, and commerce, as the secondary energy generated in the production process, accounts for 52 % of the total energy consumption [1]. In China, industrial energy consumption accounts for more than 70 % of the total energy consumption, and about 10 ~ 50 % of industrial energy consumption is converted into industrial waste heat with different carriers and temperatures [2]. If waste heat can be used effectively, it will considerably relieve the pressure on the energy demand side. According to the source temperature of waste heat, waste heat can be generally divided into three levels: high-grade waste heat (T greater than 923 K), medium-grade waste heat (503 K < T < 923 K), and low-grade waste heat (T < 503 K) [3]. High- and medium-grade waste heat can be recycled through the traditional steam Rankine cycle with a high conversion efficiency due to its high temperature level. However, for low-grade waste heat that accounts for more than 60 % of the total waste heat, the traditional steam Rankine cycle cannot be effectively applied due to the low temperature [1,4]. Considering such a large amount of low-grade waste heat, the recovery of low-grade waste heat can not only alleviate the energy crisis but also bring considerable environmental and economic benefits. Therefore, it is necessary to develop new energy recovery technology to recover low-grade waste heat.

* Corresponding author at: School of Materials Science and Engineering, University of Science and Technology Beijing, Beijing 100083, China.
E-mail address: zhanghu@ustb.edu.cn (H. Zhang).

https://doi.org/10.1016/j.applthermaleng.2022.119827
Received 10 August 2022; Received in revised form 4 November 2022; Accepted 5 December 2022
Available online 10 December 2022

Nomenclature

TMG	Thermomagnetic generator
T_C	Curie temperature (K)
H	Magnetic field (A/m)
M	Magnetization (Am^2/kg)
B	Magnetic flux density (T)
T	Temperature (K)
T_{cold}	Cold end temperature (K)
T_{hot}	Hot end temperature (K)
ρ	Density (kg/m^3)
C_P	Specific heat capacity (J/kg K)
λ	Thermal conductivity (W/m K)
C_0	Specific heat capacity ratio
C_{Pexp}	Experimental specific heat capacity (J/kg K)
C_{Psim}	Input specific heat capacity in the simulation model (J/kg K)
λ_0	Thermal conductivity ratio
λ_{exp}	Experimental thermal conductivity (W/m K)
λ_{sim}	Input thermal conductivity in the simulation model (W/m K)
MCE	Magnetocaloric effect: a heating or cooling of a magnetic material when the applied magnetic field changes.
μ_0	Permeability of vacuum ($4\pi \times 10^{-7} N/m^2$)
Φ	Magnetic flux (Wb)
U	Induced electrodynamic potential (V)
I	Induced current (A)
N	Coil turns
t	Time (s)
t_{cycle}	Cycle period (s)
S	cross-section area of coil (m^2)
R	Resistance of coil (Ω)
P_{max}	Max output power (W)
P_{avg}	Average output power (W)
P_d	Power density (W/m^3 K)
dT/dt	Temperature change rate (K/s)
dB/dt	Magnetic flux desnity change rate (T/s)
dB/dT	Magnetic flux desnity change rate with temperature (T/K)
dM/dT	Magnetization change rate with temperature (Am^2/kg K)
ΔB	Magnetic flux density change (T)

In the past few decades, various techniques have been developed to recycle the waste heat based on organic Rankine cycle (ORC) [5], thermoelectric effect [6–9], pyroelectric effect [10–12], thermoacoustic effect [13–15], and thermomagnetic effect [16–23]. The thermoelectric generators (TEGs) based on the thermoelectric effect are currently popular waste heat recovery technology, but their performance is positively correlated with temperature differences. When the waste heat temperature is lower than 200 °C, the conversion efficiency of TEGs with a lower temperature difference decreases to less than 5 % [24]. For pyroelectric technology, recent studies have shown its high power density (the power density reaches 526 W/cm^3 under a temperature change of 50 K), but its practical application is limited by its high impedance and low output current [25]. In contrast, the thermomagnetic generators (TMGs) based on the thermomagnetic effect utilize the waste heat to induce the magnetic transition of materials, and then electricity can be obtained in the coil wound around the magnetic materials due to the magnetic flux change [23]. Unlike ORC generators that may emit harmful organic matter, TMGs using magnetic materials are safer and more environmental friendly. Moreover, theoretical studies reveal that the conversion efficiency of TMGs up to 55 % of Carnot efficiency is more efficient than other technologies such as ORC generator, thermoelectric generator, and thermoacoustic Stirling generator, especially in the low-grade waste heat range [3,26]. Therefore, TMG is a very promising technology for low-grade waste heat recovery.

According to the energy conversion method, the TMGs can be divided into passive TMG and active TMG [27]. Generally, the passive TMG converts the thermal energy first into mechanical energy, and then transfers mechanical energy further into electrical energy. Chen *et al.* [28] and Song *et al.* [29] used Gd and $La_{0.85}Sr_{0.15}MnO_3$-based composites respectively as working materials to design thermal energy collection devices. The devices include permanent magnets, cantilever beams, and piezoelectric material in addition to the working materials. Under the variation of temperature and magnetic field, the devices generate self-driving vibration to convert thermal energy into mechanical energy and cooperate with piezoelectric material to realize the conversion of mechanical energy into electrical energy, thereby realizing the collection of low-grade waste heat. Gueltig *et al.* [20] made a film of $Ni_{49.5}Mn_{28}Ga_{22.5}$ and combined it with a Cu-Zn cantilever to form a TMG. The film oscillates periodically under the action of magnetic force and the elastic force of cantilever beam. During the oscillation process, the magnetic flux passing through the coil changes due to the magnetic field gradient and the change of the film magnetization, thereby generating an induced current of 180 μA. Kishore *et al.* [21] designed a linear thermomagnetic energy harvester using Gd as the working material. The device abandons the design of cantilever beam, and uses the gravity and magnetic force of block Gd to realize the periodic operation of the device. Recently Rodrigues *et al.* [30] demonstrated a hybrid device that combines the thermomagnetic and triboelectric effects. The ferromagnetic material produces periodic motion at a low-temperature difference of 30 °C through the thermomagnetic effect. This mechanical motion is then converted into electricity using a low-cost triboelectric nanogenerator (TENG). However, the current and output power generated by the above passive TMGs are relatively low due to the indirect conversion of thermal energy to electrical energy.

In contrast, the active TMG directly converts the thermal energy into electrical energy. Theoretically, active TMG shows higher efficiency and output power than those of passive TMG by avoiding the extra energy conversion (thermal energy to mechanical energy) [18,27]. Elliott et al. [31] pointed out that the theoretical efficiency limit of the active TMG could reach as high as 55 % of Carnot efficiency. However, due to the unsatisfactory material properties and device design, the experimental conversion efficiency of active TMGs is still much lower than the theoretical value so far. In recent years, different active TMGs have been designed to improve the efficiency of low-grade waste heat recovery [16,22,23,31]. Waske *et al.* [23] proposed an active TMG with a pretzel-like magnetic circuit. It not only effectively avoids the magnetic stray field in the device, but also improves the performance of the TMG by an order of magnitude. In addition, Jiang *et al.* [32] systematically studied the performance of the regenerative active TMG. However, the TMG performance was low due to the vibration of the experimental setup, the resistance of the current preamplifier, the uneven distribution of the gadolinium sheet, the severe oxidation of the gadolinium sheet, and the air gap in the assembly.

So far, poor performance of the current TMGs at low-grade temperature range still hinders the application of this novel technology. In addition to the magnetic circuit design, the performance of the TMG is significantly affected by the key device parameters (sample cabin size, system temperature range, and cycle period) and material properties (thermal conductivity and specific heat capacity). However, to our best knowledge, there is still a lack of systematic research in this regard. As such, there is an urgent need to investigate the effect of key parameter from an actual design point of view. Recently, we built an active TMG for low-grade waste heat recovery and studied the TMG performance of typical magnetocaloric effect (MCE) materials Gd and $La(Fe, Si)_{13}$-based

composite [33]. In present work, for the first time, we further systematically study the effects of different key device and material parameters on the TMG performance through a combination of experiment and simulation. The performance of present TMG is improved significantly by optimizing the key device parameters including sample cabin size, system temperature range, and cycle period. Particularly, the improved instantaneous maximum power density is one order of magnitude higher than the experimental value before the optimization, and even three orders of magnitude higher than those of other reported TMGs [22,28,32].

2. Experimental methodology

2.1. Experimental setup

Fig. 1 show the experimental setup of the active TMG in present study. As shown in Fig. 1(a), The active TMG consists of the Halbach permanent magnetic, sample cabin, TMG material and the auxiliary system (hot and cold water pump, control panel, and data collection system). A 3D printed sample cabin is placed in the center of a hollow cylindrical Halbach permanent magnet which provides a radial magnetic field of ~ 1 T (Fig. 1(b)). The magnetic field of the Halbach permanent magnet was measured by a gaussmeter. The TMG sample is placed behind a fence in the sample cabin, and so the sample would not be flushed away by the heating/cooling fluid flowing in from the upper side of the sample cabin (Fig. 1(c, d)). Then, the copper coil with N = 300 turns is wound around the sample cabin (Fig. 1(e)). Such a sample cabin design not only realizes the direct heat transfer between the fluid and material, but also avoids the complex geometric design and high requirement of mechanical property for the TMG materials in comparison with other TMGs [16].

Fig. 1(f,g) shows the working principle of the TMG during the (d) heating and (e) cooling processes, respectively. The ice water (~273 K) and boiled water (~373 K) are pumped from the storage barrels and controlled to alternatively flow through the sample cabin with a flow rate of 0.05 L/s. Each heating/cooling time is 30 s. The water temperature in the sample cabin becomes to be ~ 288 K (cold end) and ~ 353 K (hot end) after flowing through the pump and pipes. This working temperature range (288 ~ 353 K) of present TMG is suitable for the low-grade waste heat recovery. As shown in Fig. 1(f), the boiled water flows through the sample cabin and heats the TMG material to above its T_C, which leads to the magnetic transition of TMG material from ferromagnetic (FM) state to paramagnetic (PM) state, and then causes the reduction of magnetic flux in the coil, thus inducing a current in the coil. On the contrary, the TMG material would transform from PM back to FM state when the ice water flows through, which then results in an inverse induced current (Fig. 1(g)). Consequently, the TMG could continuously convert the low-grade waste heat into alternating current by cycling the heating and cooling processes. The experimentally induced I was measured in the short-circuit mode by using a data collection system (RIGOL M300).

According to the Faraday's law, the induced electrodynamic potential (U) is determined by the change rate of magnetic flux ($d\Phi/dt$) in a N turns of coil [18,34].

$$U = -N\frac{d\Phi}{dt} \tag{1}$$

Then, the induced current I can be obtained as follows,

$$I = \frac{U}{R} = -\frac{NS}{R}\frac{\mathrm{d}B}{\mathrm{dt}} = -\frac{NS}{R}\frac{\mathrm{d}B}{\mathrm{d}T}\frac{\mathrm{d}T}{\mathrm{dt}} \tag{2}$$

where R is the resistance of coil, S is the cross-section area of coil, and t is time. dB/dt is the change rate of magnetic flux density with time. dB/dT is the change rate of magnetic flux density with temperature. dT/dt is the temperature change rate with time. The first term NS/R is related to the TMG device, while the terms of dB/dT and dT/dt are related to the properties of TMG materials.

2.2. Material preparation and characterization

Gadolinium (Gd) metal has been considered as the benchmark material for MCE, and has also been used as a typical working material in many TMGs [35–37]. Thus, Gd is used as the working material in present active TMG. The Gd metal (>99.95 wt%) was purchased from a commercial vendor and then cut into cylindrical pieces of Φ10 × 5 mm by wire-cutting. The magnetization M and specific heat C_P were measured using a cryogen-free, cryocooler-based physical property measurement system (VersaLab) from Quantum Design Inc. The density of sample was measured by Archimedes method.

Fig. 2(a) shows the temperature dependences of zero-field-cooling (ZFC) and field-cooling (FC) magnetization (M) under 1 T for Gd metal. The Gd experiences a magnetic transition from FM to PM state around T_C = 292 K, defined as the peak value of the change rate of magnetization with temperature dM/dT (inset of Fig. 2(a)). This T_C is within the working temperature range (288 ~ 353 K) of our active TMG. According to Eq. (2), the induced current I is proportional to dB/dT, and thus the I is also proportional to dM/dT since $B \propto M$. Therefore, the larger dM/dT at T_C would be beneficial to obtaining higher induced I

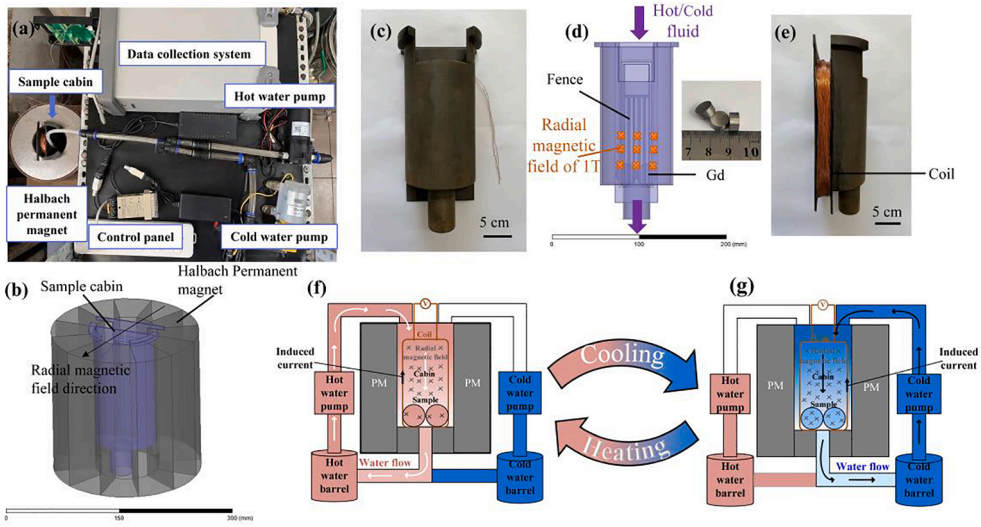

Fig. 1. The experimental setup of the active TMG in present study. (a). The photo of the home-built active TMG. (b). A 3D printed sample cabin is placed in the center of a hollow cylindrical Halbach permanent magnet which provides a radial magnetic field of ~ 1 T. (c, d) The photo and schematic diagram of the sample cabin, and the TMG sample is placed behind a fence in the sample cabin. (e) Side of the sample cabin. The copper coil with N = 300 turns is wound around the sample cabin. Working principle of the TMG during the (f) heating and (g) cooling processes, respectively.

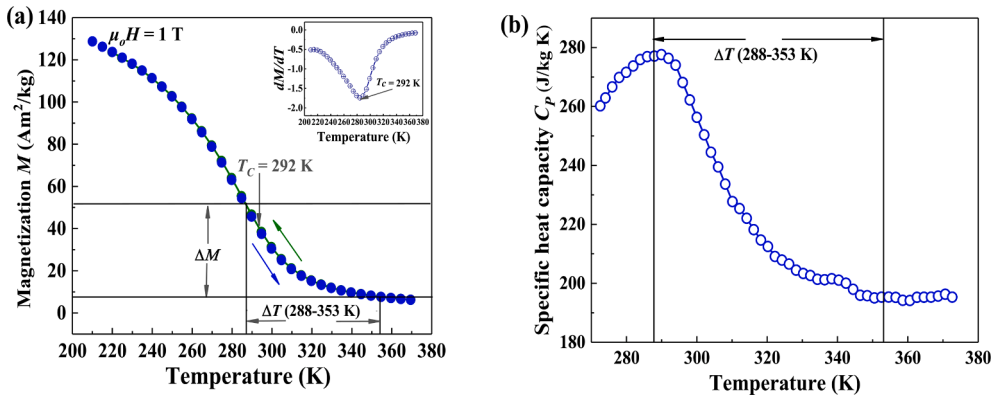

Fig. 2. (a) Temperature dependences of ZFC and FC magnetization under 1 T for Gd metal. The inset shows the corresponding *dM/dT-T* curve derived from the *M*−*T* curves. (b) Temperature dependence of C_P in zero field for Gd.

value. Moreover, no thermal hysteresis is observed between the ZFC and FC curves, corresponding to the typical second-order magnetic transition. This perfectly reversible magnetic transition is favorable for practical application since it would not cause the discrepancy of working temperatures during the heating and cooling processes. In addition to *dM/dT*, the *dT/dt* also affects the *I* value according to Eq. (2). Generally, a large *dT/dt* is expected in the materials with small specific heat capacity (C_P) and large thermal conductivity (λ). Fig. 2(b) shows the temperature dependence of C_P in zero field for Gd. The C_P reaches the peak of ~ 276.3 J/kg K at T_C, and then decreases gradually with the increase of temperature. The C_P of Gd metal is lower than those of other typical room temperature MCE materials, such as La(Fe, Si)$_{13}$-based alloys [38–40] and NiMn-based Heusler alloys [41,42]. Besides, the λ of Gd increases from ~ 9.4 W/m K near 288 K to ~ 12.2 W/m K near 353 K [43], which is significantly higher than those of other typical MCE materials, such as La(Fe, Si)$_{13}$-based alloys [40,43], $Gd_5(Si, Ge)_4$ alloys [44], and MnAs [44]. This low C_P and high λ of Gd metal are favorable to acquiring high TMG performance.

3. Numerical simulation

3.1. Numerical model

A 3D numerical model was developed based on the experimental geometry (Fig. 1(a)) using COMSOL Multiphysics software to investigate the active TMG. The relevant parameters of TMG used in the numerical model are listed in Table 1. We used the heat transfer module and magnetic field module to simulate the temperature change of the TMG material and the induced current generated by the TMG. The simulated current was compared with the measured current to verify the accuracy of the model. Then the effects of different key devices (sample cabin size, system temperature range, and cycle period) and material parameters (thermal conductivity, and specific heat capacity) on the TMG performance are analyzed systematically by the numerical model.

Table 1
The relevant parameters of TMG used in the numerical model.

Model parameters	Symbol	Value
device parameters		
system temperature ranges	T_{cold} ~ T_{hot}	288 ~ 353 K
flow rate	–	0.5 L/s
number of turns	*N*	300
total resistance	*R*	15 Ω
sample mass	m	6.2 g
cycle period	–	60 s
properties of Gd		
magnetic property	*M*	Fig. 2(a)
thermal conductivity	λ	Ref. [43]
specific heat capacity	C_P	Fig. 2(b)
density	ρ	7610 kg/m
magnetic properties of NdFeB		
coercivity	H_{cB}	1036 kA/m
relative permeability	μ_r	1.056

3.2. Governing equations

The key of numerical simulation is to solve the governing equation. The numerical model includes heat transfer module and magnetic field module, so the corresponding governing equations need to be solved to obtain numerical results.

(1) Heat transfer equation

The heat diffusion equation was used to describe the heat transfer in solids, which is given as [21]:

$$\rho C_P \frac{\partial T}{\partial t} - \nabla \cdot (\lambda \nabla T) = Q \tag{3}$$

where ρ, C_P, λ, and *T* are density, specific heat capacity, thermal conductivity, and temperature, respectively. *Q* represents the heat absorbed or released by the TMG material in contact with the fluid.

(2) Magnetic field equation

The governing equation describing the magnetic field is expressed as:

$$\nabla \times E = -\frac{\partial B}{\partial t} \tag{4}$$

where *E*, *B*, and *t* are electrical field, magnetic flux density, and time, respectively.

The temperature curve of Gd metal with time was obtained by solving the heat transfer equation, and the *E* of the TMG was obtained by combining the *M*−*T* curve (Fig. 2(a)) and solving the above magnetic field equation. Then, the induced current of TMG can be obtained by Eq. (2).

3.3. Boundary conditions and initial conditions

Fig. 3(a) presents the numerical simulation model of the TMG. In the numerical model, the TMG is surrounded by an air domain. A magnetic insulation boundary condition is applied to the edge of the air domain. It represents the boundary where the tangential magnetic field vanishes to zero and can be expressed as:

$$n \times H = 0 \tag{5}$$

where *n* and *H* represent the normal vector and magnetic field strength

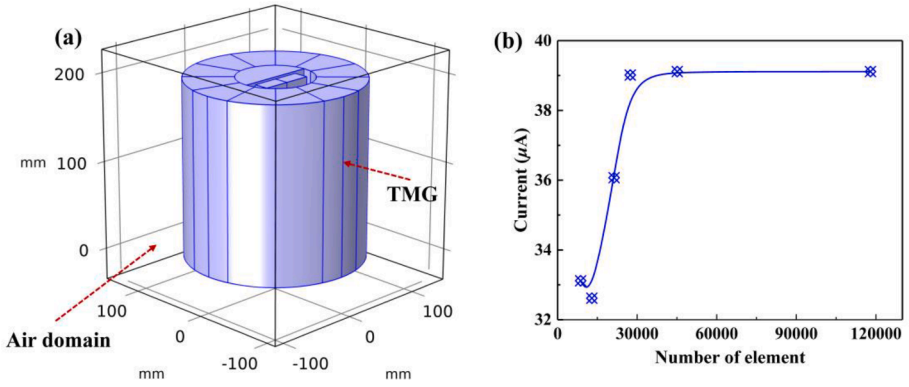

Fig. 3. (a) The numerical simulation model of the TMG. (b) Simulated induced current of the TMG as a function of the number of mesh elements.

of the boundary, respectively.

For the heat transfer module, the cold side temperature is 288 K and the hot side temperature is 353 K. The initial value for all the domain temperatures is considered as the ambient temperature of 293.15 K except the hot and cold ends. Meanwhile, the boundary conditions for the regions in the TMG are set as thermal insulation except the sample. This boundary condition means that there is no heat flux across the boundary.

3.4. Mesh independence test

To ensure the accuracy of the numerical model and minimize the computation time, mesh-independent tests were performed using free tetrahedral mesh elements. Extra-coarse (8754 mesh elements), coarser (12968 mesh elements), coarse (21377 mesh elements), normal (27477 mesh elements), fine (45198 mesh elements), and finer (118178 mesh elements) were tested. Fig. 3(b) shows the simulated induced current of the TMG as a function of the mesh elements. The induced current of the TMG reaches saturation when the number of mesh elements reaches 45198. Therefore, we selected fine mesh elements for the subsequent simulation, because it would ensure the calculation accuracy and also reduce the computing resources and computing time as much as possible.

4. Results and discussion

4.1. Performance of the TMG

Fig. 4(a) shows the induced current *I* generated by the TMG during the heating and cooling cycles. A positive *I* peak of 28.8 μA is obtained during the heating cycle due to the FM-PM magnetic transition, while a negative *I* peak of − 12.2 μA is generated during the cooling cycle due to the reverse magnetic transition. It is noted that the *I* during heating is much higher than the one during cooling. In order to understand the difference of *I* values during the cycles, the finite element method with COMSOL simulation is used based on the experimental parameters

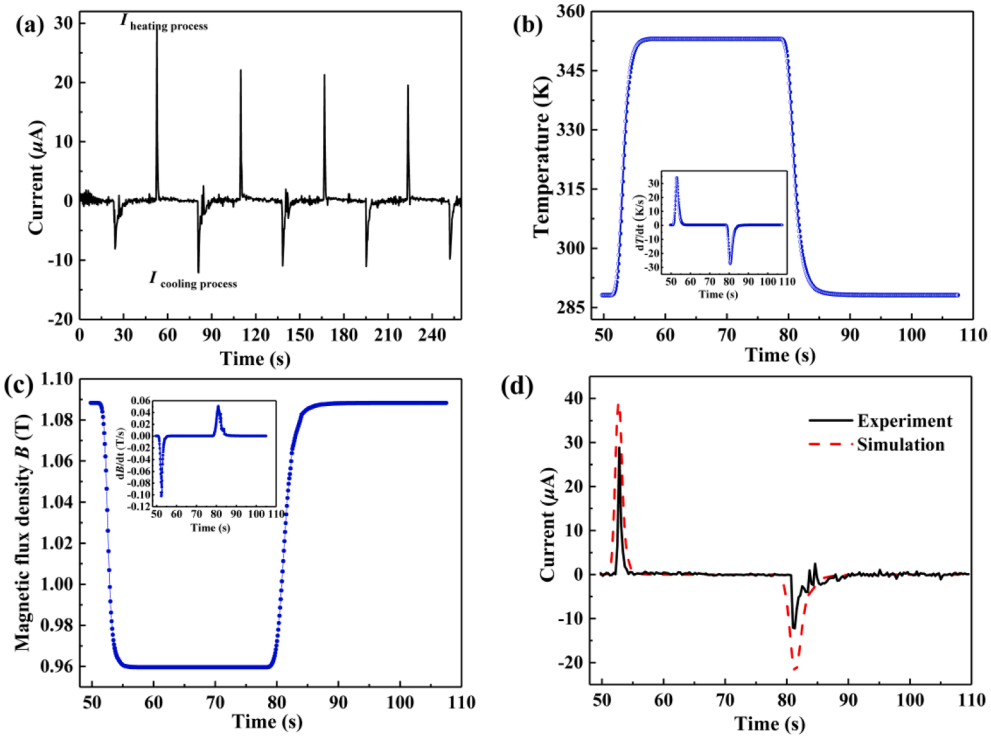

Fig. 4. (a) Induced current *I* generated by the TMG during the heating and cooling cycles. (b) Simulated sample temperature as a function of time. The inset shows the corresponding *dT/dt-t* curve derived from the *T-t* curves. (c) Time dependence of simulated magnetic flux density *B* during one cycle. The inset shows the corresponding *dB/dt-t* curve derived from the *B-t* curves. (d) Comparison of experimental and simulated *I-t* curves during one heating and cooling cycle.

(Table 1). Fig. 4(b) shows the simulated sample temperature as a function of time. The sample temperature increases significantly from 288 K to ~ 353 K within the first 6 s due to the large temperature difference between the sample and heating medium, and then it remains constant until the cooling cycle. Similarly, the sample temperature drops sharply at the beginning of cooling and then becomes constant during the rest of cooling process. The inset of Fig. 4(b) shows the temperature change rate with time curves. The maximum temperature change rate with time dT/dt appears at the first 3 s during both heating and cooling processes. This fact reveals that the magnetic transformation would be completed in the first few seconds, and so the cycle period could be shortened to improve the TMG performance. Furthermore, the time dependence of magnetic flux density B is simulated based on the T-t curves and is shown in Fig. 4(c). The B also changes largely at the beginning of each heating/cooling cycle due to the thermal-induced magnetic transition. The corresponding magnetic flux density change rate with time dB/dt is obtained as shown in the inset of Fig. 4(c). It is seen that the maximum dB/dt during the heating is − 0.1 T/s, much higher than the dB/dt of 0.05 T/s during the cooling. Since the TC of Gd (292 K) is close to the cold end temperature (288 K), the magnetic transition would occur earlier during the heating process than that during the cooling, which then leads to a higher dB/dt during the heating due to the faster temperature change dT/dt at the beginning of each cycle. This higher dB/dt causes the larger I during the heating than the I during the cooling according to the $I \propto dB/dt$. The simulated I is obtained based on the B-t curve according to the Faraday's law, and Fig. 4(d) compares the simulated I-t curve with the experimental result during the first cycle. The simulation shows a similar I-t profile with the experimental curve, but the peak value is higher than the experimental one. The mean difference between the simulation and experimental results is estimated to be 13.5 μA with a standard deviation of 3.8 μA. This discrepancy between experimental and simulation results is likely due to the lower experimental dT/dt, which is caused by the following reasons: 1) the imperfect thermal conduction between the sample and the heating/cooling water in the experiment, 2) the large temperature gradient from the surface to the center of the bulk sample, and 3) the presence of residual heat in the sample cabin during the cycle. Moreover, with the increase of cycling, above reasons would make the sample temperature not be able to return to the initial temperature, and so the narrower working temperature range would result in the further reduction of temperature rate. Thus, the I value decreases gradually with increasing cycles, as shown in Fig. 4(a). It should be pointed out that, although there is a discrepancy between the simulation and experimental results, both simulation and experimental results exhibit the similar trends with the variation of key parameters in the following study.

In addition to induced current I, the output power P and power density P_d are also important indicators that reflect the performance of the TMG. Based on the I-t curve, the instantaneous maximum output power P_{max} and average power P_{avg} of the TMG can be obtained using

$$P_{max} = I_{max}^2 \cdot R \tag{6}$$

$$P_{avg} = \frac{1}{t_{cycle}} \cdot \int_t^{t + t_{cycle}} I(t)^2 \cdot R dt \tag{7}$$

where I_{max} is the maximum I in a cycle, R is the resistance of coil (15 Ω), t is the time, and t_{cycle} is the time required for one cycle. The P_{max} and P_{avg} are calculated to be 8.3 nW and 0.4 nW, respectively. The corresponding power density P_d is calculated by dividing the output power by the volume of the sample and the temperature difference between cold end and hot end. The maximum P_d and average P_d are 0.16 mW/m^3 K and 0.01 mW/m^3 K, respectively. This power density is much lower than those of other reported TMGs (W/m^3 K), and so it indicates that the present TMG needs to be further optimized to improve the performance.

4.2. Effects of key parameters

Although the present TMG fits well with the low-grade waste heat recovery, the above result reveals that its performance is still very low and has a large potential to be improved. Some key device and sample parameters have a significant influence on the TMG performance. Thus, the effect of some key parameters, including sample cabin size, system temperature range, cycle period, thermal conductivity, and specific heat capacity (listed in Table 1), has been studied systematically based on the finite element simulation to improve the TMG performance.

(1) Sample cabin size

It is well known that $B = \Phi/S$, where Φ is magnetic flux and S is the area enclosed by the coil. When the Φ is fixed, the smaller the S is, the higher the B is. Thus, the smaller cabin size means a smaller S, which would be desirable to higher TMG performance. In order to study how strongly the cabin size affects the TMG performance, the height of sample cabin is tuned and the corresponding simulated I-t curves are obtained as shown in Fig. 5(a). The I during both heating and cooling processes increases remarkably with the reduction of the sample cabin height. But the I during the heating is more sensitive than the one during the cooling to the change of cabin size. According to $I \propto (dB/dT)(dT/dt)$, the reduction of cabin size would increase the dB, thus leading to the enhancement of I. In addition, since the magnetic transition occurs earlier during the heating process than that during the cooling, the dT/dt around TC during the heating is higher than that during the cooling, which results in a larger variation of I. Fig. 5(b) plots the peak I value and the decrease ratio of area S as a function of the sample cabin height. It is seen that the variation of I is in a good agreement with the variation of S, confirming that the reduction of cabin size improves the TMG performance. Moreover, the decrease ratio of S becomes higher with the decrease of the sample cabin height, resulting in the larger enhancement of I. This fact suggests that the TMG performance would be more sensitive to the cabin size at the small scale.

(2) System temperature range (T_{cold}-T_{hot})

In our previous work, system temperature range (T_{cold}-T_{hot}) has been revealed to affect the TMG performance largely [33]. Fig. 6 shows the (a) experimental and (b) simulated induction current I at same T_{hot} = 353 K but different T_{cold}. Although the experimental I values are lower than the simulated ones, both results show the similar trends with the variation of T_{cold}. The I increases remarkably with the decrease of T_{cold} during both heating and cooling processes. Fig. 6(c) shows the simulated T-t curves of Gd at same T_{hot} = 353 K but different T_{cold}. As the T_{cold} decreases, the system temperature range expands towards the lower temperature range, thus making the temperature of Gd vary more rapidly. As shown in the inset of Fig. 6(c), the temperature change rate dT/dt of Gd increases with the reduction of T_{cold}. Furthermore, Fig. 6(d) shows the corresponding B-t curves at same T_{hot} = 353 K but different T_{cold}. Due to the faster temperature variation, the magnetic flux density B drops more sharply with the decrease of T_{cold}. Moreover, the change in magnetic flux density ΔB increases significantly with the decrease of T_{cold}. This is because the lower T_{cold} would strengthen the FM state of Gd, resulting in the larger ΔB between T_{hot} and T_{cold}. Therefore, the B varies not only more rapidly but also more largely by lowering the T_{cold}, leading to an increase of dB/dt correspondingly (inset of Fig. 6(d)). Consequently, the I increases with the decrease of T_{cold} according to the $I \propto dB/dt$.

On the other hand, Fig. 6(e) and 6(f) show the experimental and simulated induction current I at same T_{cold} = 288 K but different T_{hot}. The experimental and simulated I values also show the similar trends with the variation of T_{cold}, that is, the I increases with the increase of T_{hot} during the heating process. But the enhancement is not as large as that with the variation of T_{cold}. Meanwhile, the I during the cooling process

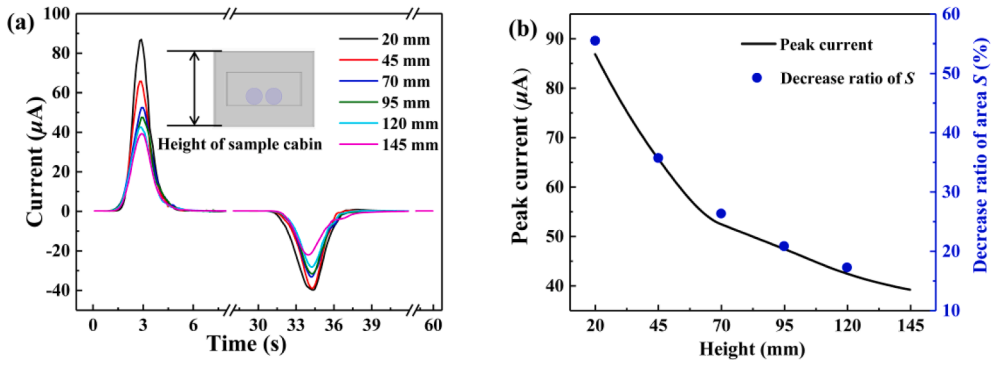

Fig. 5. Effect of different sample cabin sizes on the performance of the TMG. (a) The simulated *I-t* curves with different sample cabin sizes. The inset shows a schematic diagram of the sample cabin height. (b) The peak *I* value and the decrease ratio of area *S* as a function of the sample cabin height.

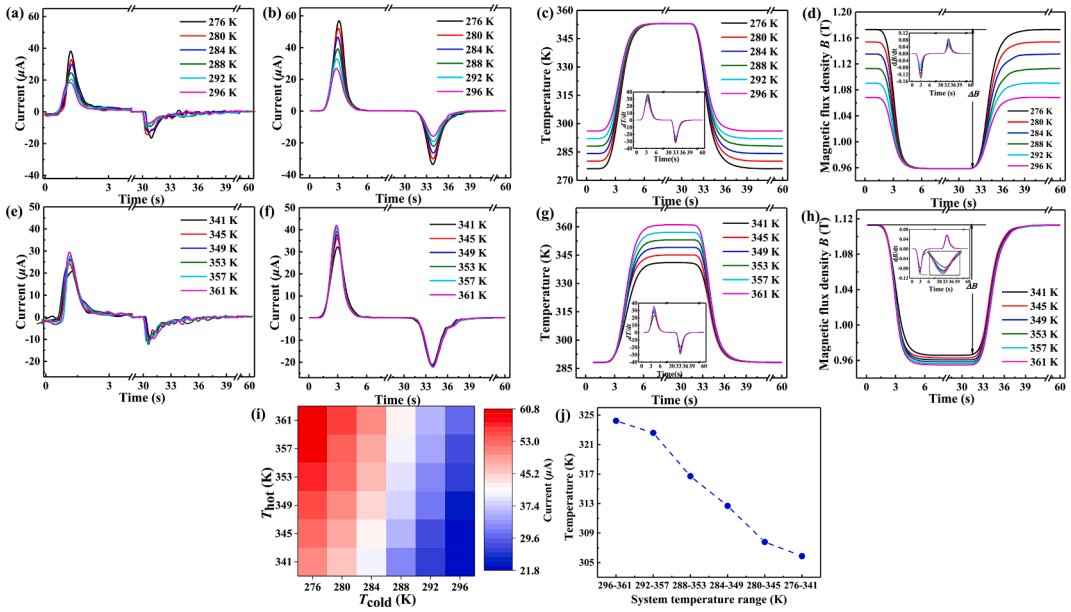

Fig. 6. (a) Experimental *I-t* curves, (b) Simulated *I-t* curves, (c) Simulated *T-t* curves, and (d) Simulated *B-t* curves of Gd at same $T_{hot} = 353$ K but different T_{cold}. (e) Experimental *I-t* curves, (f) Simulated *I-t* curves, (g) Simulated *T-t* curves, and (h) Simulated *B-t* curves of Gd at same $T_{cold} = 288$ K but different T_{hot}. The insets show the corresponding *dT/dt-t* and *dB/dt-t* curves. (i) The simulated peak *I* value as a function of T_{hot} and T_{cold}. (j) The temperature corresponding to the maximum *dT/dt* as a function of system temperature range.

remains constant with the increase of T_{hot}. Fig. 6(g) shows the simulated *T-t* curves of Gd at same $T_{cold} = 288$ K but different T_{hot}. Similar to Fig. 6(c), the temperature of Gd varies more rapidly with the system temperature range expanding towards the higher temperature range. The maximum *dT/dt* of Gd increases with the increase of T_{hot} as shown in the inset of Fig. 6(g). Fig. 6(h) shows the corresponding *B-t* curves at same $T_{cold} = 288$ K but different T_{hot}. Since the initial T_{hot} is much higher than $TC = 292$ K, the Gd at T_{hot} is already in PM state and the *M* and *B* are very low. Then, the further increase of T_{hot} could not result in a larger reduction of *B*. As shown in the inset of Fig. 6(h), the maximum *dB/dt* during the heating increases slightly while the one during the cooling remains constant with the increase of T_{hot}, which corresponds to the behavior of *I* value. Considering that $dB/dt = (dB/dT)(dT/dt)$, the *dB/dT* would not be affected by the change of T_{hot}, and so the *dB/dt* would be determined by *dT/dt*. It is seen from Fig. 6(g) that the *dT/dt* at *TC* during the heating increases gradually while the one during the cooling remains almost same, thus leading to the increase of *dB/dt* during the heating while constant *dB/dt* during the cooling.

Fig. 6(i) plots the simulated peak *I* value as a function of T_{hot} and T_{cold}. The maximum peak *I* can be obtained at the lowest T_{cold} and highest T_{hot}. On the contrary, the minimum peak *I* is obtained at the highest T_{cold} and lowest T_{hot}. This fact reveals that the larger system temperature range is favorable to the improvement of TMG performance. In addition, when the temperature difference is fixed at 65 K, peak *I* increases with the system temperature range shifting from the high temperature-range (296 ~ 361 K) to the low-temperature range (276 ~ 341 K). Considering that $I \propto (dB/dT)(dT/dt)$, the largest *I* can be obtained when both *dB/dT* and *dT/dt* reach the highest values. Generally, the highest *dB/dT* is reached at T_C. Then, the largest *I* would be achieved if the maximum *dT/dt* is also obtained at T_C. Fig. 6(j) shows the temperature corresponding to the maximum *dT/dt* as a function of system temperature range. It is found that the temperature corresponding to the maximum *dT/dt* reduces and gradually approaches the T_C of Gd with the system temperature range shifting towards lower temperatures, thus leading to the increase of peak *I* value. Consequently, large system temperature range with the maximum *dT/dt* occurring around T_C is favorable to the improvement of TMG performance.

(3) Cycle period

As mentioned above, the magnetic transition would be completed in the first few seconds, and so the TMG performance could be improved by

shortening the cycle period. Fig. 7 shows the (a) experimental and (b) simulated *I*–*t* curves under different cycle periods. Due to the imperfect thermal conduction, the experimental results show relatively unstable and lower values than the simulated results, but both results still show similar trends with the change of cycle period. The *I* value remains nearly same for all cycle periods except the shortest cycle of 5 s. It is seen that the *I* peak is completed within the first 6 s of each heat transfer process, and then followed by a stable baseline. However, the *I* peak is not finished when the cycle period is 5 s, implying the incomplete magnetic transition. Fig. 8 shows the simulated *T*-*t* curves under different cycle periods. It is seen that T_{hot} of Gd only reaches ~ 342.2 K and the T_{cold} cannot return to the initial temperature when the cycle period is 5 s. This result indicates that the cycle period of 5 s is too short to reach a stable temperature equilibrium between Gd and the heating/cooling fluid, causing the incomplete magnetic transition. When the cycle period is larger than 5 s, both T_{hot} and T_{cold} reach the maximum, and a temperature platform appears gradually, indicating the stable temperature equilibrium. Based on the *I*-*t* curves, the average power density P_d under different cycle periods can be obtained by Eq. (7).

Fig. 9 displays the simulated peak *I* and average P_d as a function of cycle period. The peak *I* increases significantly when the cycle period increases higher than 5 s, and then remains stable around 39.3 μA with further increasing cycle period, proving that the magnetic transition can be completed within the first 6 s. Besides, the average P_d increases largely with the reduction of cycle period because more *I* peaks can be obtained. But it drops slightly when cycle period is 5 s, which is due to the decrease of *I*. Consequently, above results indicate that the cycle period could be shortened to be not less than 6 s to obtain more *I* peaks and high average P_d.

(4) Thermal conductivity

As mentioned above, large λ and small C_P are desired to obtain large dT/dt. The λ could be adjusted by composition regulation, adding high λ phase, or introducing porosity. Here, we define the thermal conductivity ratio as $\lambda_0 = \lambda_{sim}/\lambda_{exp}$, where λ_{sim} is the input thermal conductivity in the simulation model and λ_{exp} is the experimental thermal conductivity of Gd. Fig. 10(a) shows the simulated *I*–*t* curves with different λ_0. The maximum *I* increases gradually from 32.8 μA at $\lambda_0 = 0.3$ to 40.8 μA at $\lambda_0 = 2$, and then the *I* does not increase distinctly with the further increase of λ_0. Fig. 10(b) shows the simulated *T*–*t* curves with different λ_0. The temperature of Gd changes faster with the increase of λ_0, and the time between the T_{cold} and T_{hot} reduces from 6.6 s to 5.9 s with the λ_0 increasing from 0.3 to 2. With the further increase of λ_0, the *T*–*t* curves remain almost unchanged, suggesting that the temperature change rate reaches the maximum limit when $\lambda_0 > 2$, as shown in the inset of Fig. 10(b). Fig. 10(c) shows the corresponding simulated *B*–*t* curves with different λ_0. The *B* changes faster with the increase of thermal conductivity, and the dB/dt also reaches the maximum limit when $\lambda_0 > 2$ as shown in the inset of Fig. 10(c), which results in the stable *I* values. This result suggests that the increase of thermal conductivity has a limited effect on the improvement of TMG performance.

(5) Specific heat capacity

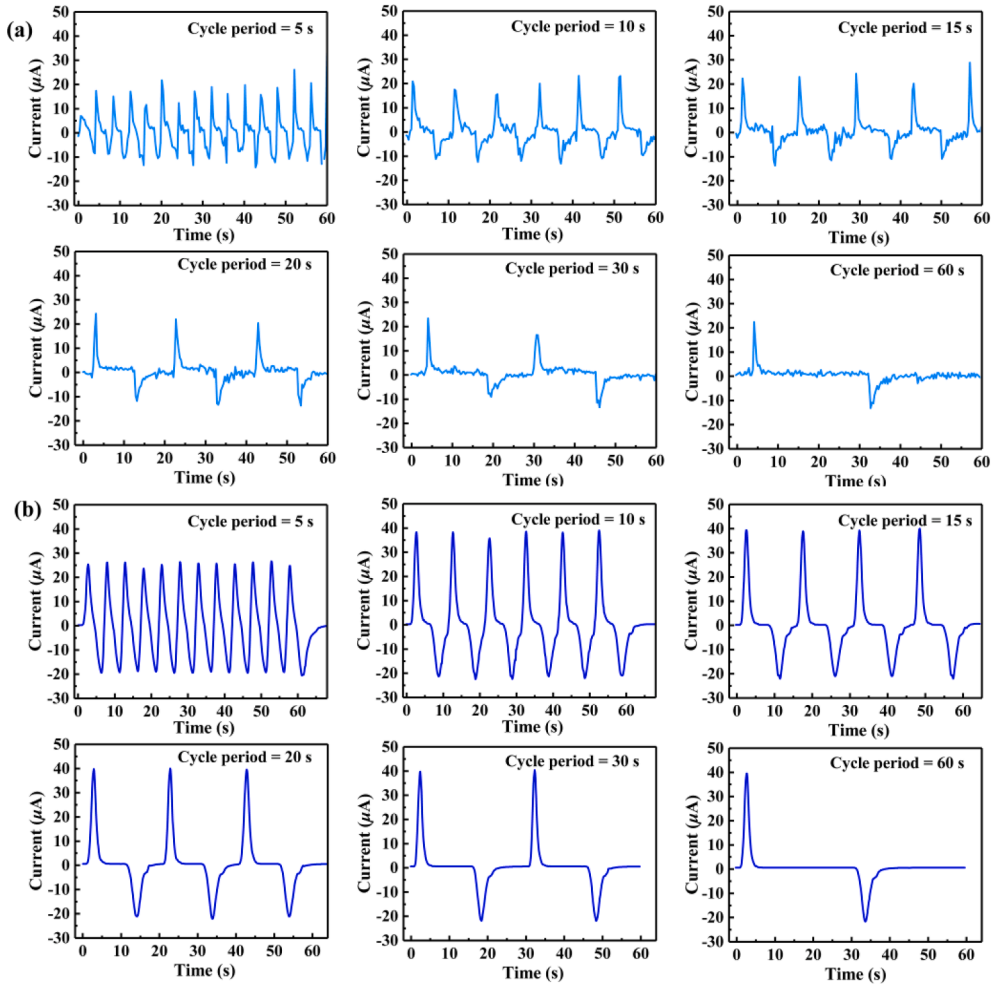

Fig. 7. (a) Experimental and (b) Simulated *I*–*t* curves under different cycle periods of 5 s, 10 s, 15 s, 20 s, 30 s, and 60 s, respectively.

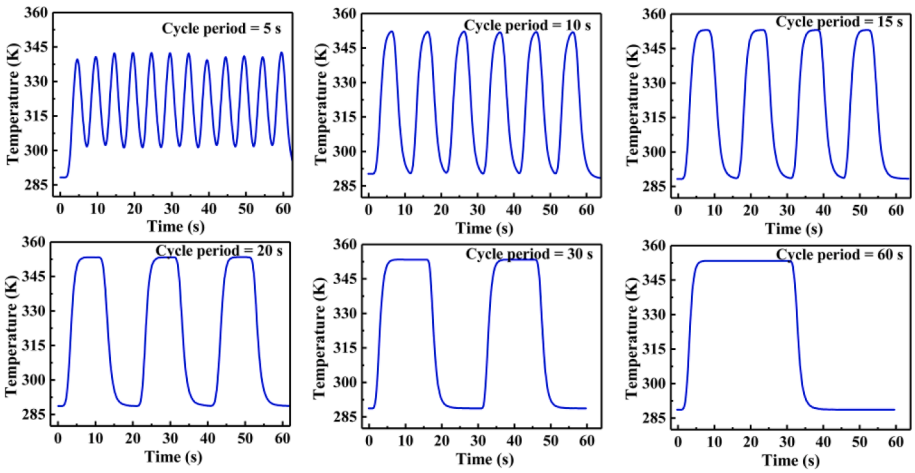

Fig. 8. Simulated *T*–*t* curves under different cycle periods of 5 s, 10 s, 15 s, 20 s, 30 s, and 60 s, respectively.

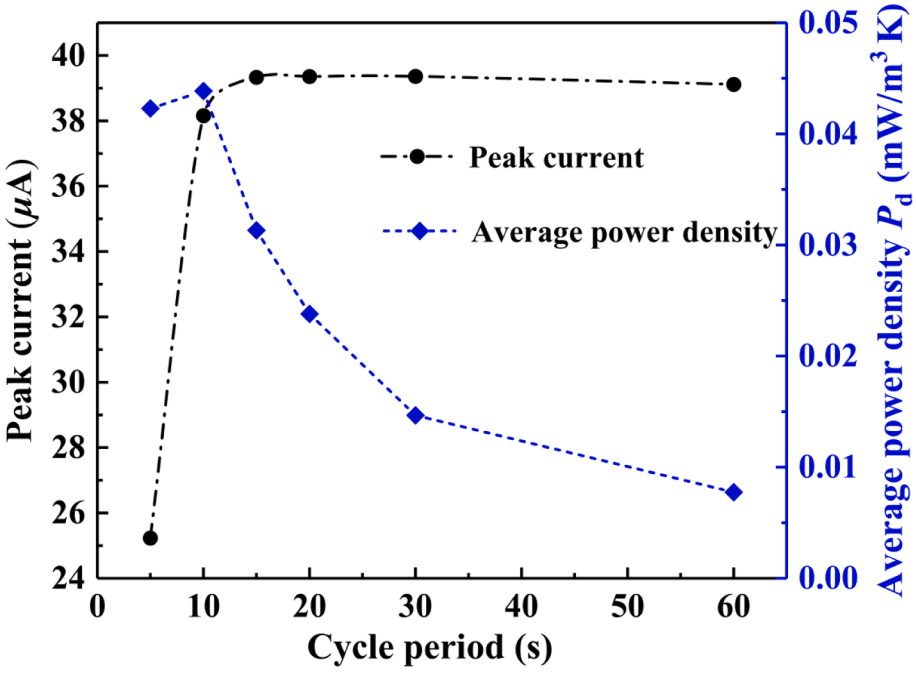

Fig. 9. The simulated peak *I* and average power density P_d as a function of cycle period.

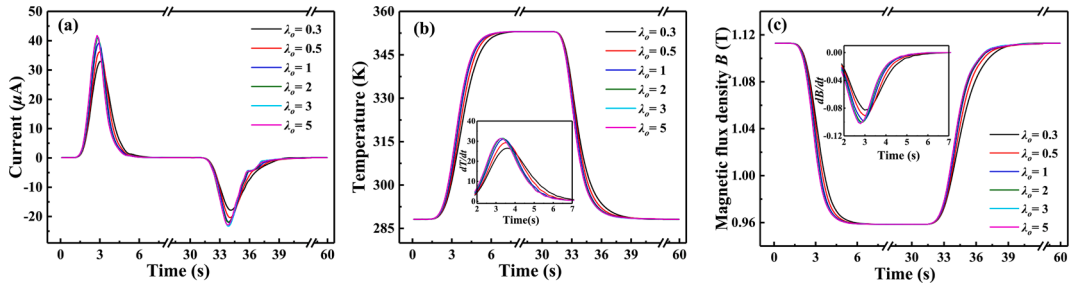

Fig. 10. (a) Simulated *I*-*t* curves, (b) *T*-*t* curves, and (c) *B*-*t* curves of Gd with different thermal conductivity ratio λ_0. The insets show the corresponding *dT*/*dt*-*t* and *dB*/*dt*-*t* curves.

Similarly, we define the specific heat capacity ratio as$C_0 = C_{Psim}/C_{Pexp}$, where C_{Psim} is the input specific heat capacity in the simulation model and C_{Pexp} is the experimental specific heat capacity of Gd. Fig. 11(a) shows the simulated *I*–*t* curves with different C_0. The *I* increases gradually with the C_0 decreasing from 5 to 1, proving that the lower C_P is favorable to the high TMG performance. With the further reduction of C_0, the *I* also does not increase largely, reaching the maximum limit. Fig. 11(b) shows the simulated *T*–*t* curves with different

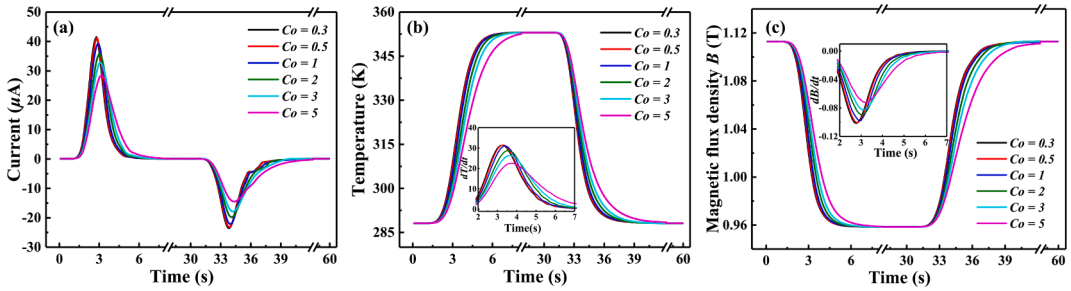

Fig. 11. (a) Simulated *I-t* curves, (b) *T-t* curves, and (c) *B-t* curves of Gd with different specific heat capacity ratio C_0. The insets show the corresponding *dT/dt-t* and *dB/dt-t* curves.

C_0. The lower C_P results in the faster temperature change, and so the temperature of Gd changes faster and the time between the T_{cold} and T_{hot} reduces from 7.7 s to 6 s when C_0 decreases from 5 to 1. The *T–t* curves do not change much with the further decrease of C_0, and the *dT/dt* reaches the maximum limit when $C_0 < 1$, as shown in the inset of Fig. 11 (b). Correspondingly, Fig. 11(c) shows the simulated *B–t* curves with different C_0. The *B* changes faster with the reduction of C_0, and so the *dB/dt* increases and reaches the maximum limit when $C_0 < 1$, as shown in the inset of Fig. 11(c). Thus, this behavior of *dB/dt* corresponds to the behavior of *I* value. This result indicates that the decrease of specific heat capacity has a similar effect as the increase of thermal conductivity, which is beneficial to the improvement of TMG performance but has a limited effect.

4.3. Optimization of TMG performance

Based on above study, we further investigate how strongly the different parameters affect the TMG performance. Fig. 12 summarizes the change rate of peak *I* value as a function of the change rate of different parameters. It is found that the change of cabin size has a strong impact on the *I*, e.g., a 100 % change rate of cabin size could enhance the change rate of peak *I* by more than 20 %. Thus, the lowest height of sample cabin of 20 mm is chosen as the optimized cabin size parameter. The expansion of system temperature range also improves the TMG performance largely. Therefore, the optimized system temperature range is chosen to be 276 ~ 361 K based on Fig. 6. The peak *I* remains nearly unchanged by shortening the cycle period until<10 s, and so the cycle period of 10 s is chosen to obtain more *I* peaks and higher P_d. For λ, a 100 % change rate of λ could increase the change rate of peak *I* by ~ 15 % at first, and then improvement reduces gradually and reaches the saturation with the further increase of λ. In addition, the reduction of C_P improves the *I* significantly, e.g., a 10 % reduction rate of C_P could enhance the change rate of peak *I* by more than 4 %. However, it is found from the inset of Fig. 12 that the improvement reduces to saturation when the change rate reaches 100 %. Consequently, the above result demonstrates that the TMG performance is influenced largely by both device and material parameters, especially the cabin size and C_P. Since it is much easier to change the device parameters than the material parameters, we keep the parameters of Gd unchanged and use the optimized device parameters (listed in Table 2) to compare the TMG performance before and after the optimization.

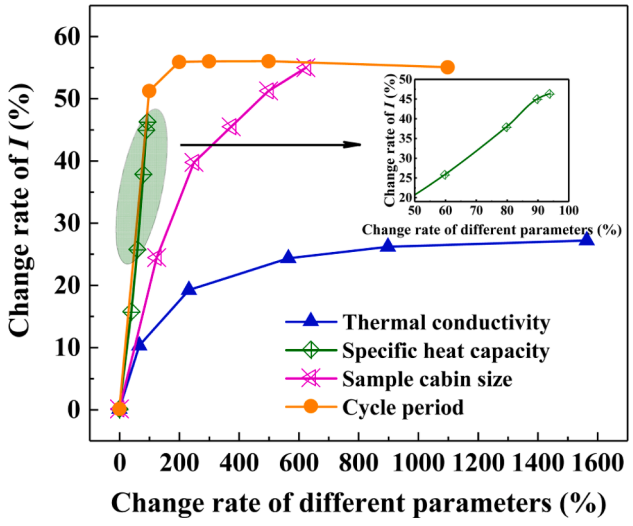

Fig. 12. The change rate of peak *I* value as a function of the change rate of different parameters. The inset shows a partial enlargement of the specific heat capacity curve.

Fig. 13 compares the *I-t* before and after optimization. In comparison with the experimental result before optimization, the simulation result indicates that the positive *I* peak during the heating increases significantly from 28.8 μA to 136.1 μA, and the negative *I* peak during the cooling increases from − 12.2 μA to − 65.0 μA after the optimization. In addition, more *I* peaks are obtained by shortening the cycle period. The P_{max} and P_{avg} are calculated to be 185.2 nW and 20.5 nW, respectively. The corresponding maximum power density P_d and average P_d are 3.6 mW/m^3 K and 0.4 mW/m^3 K, respectively, which are one order of magnitude higher than the values before optimization (0.16 mW/m^3 K and 0.01 mW/m^3 K). This result proves the remarkable improvement of TMG performance by optimizing the key device parameters. This improved TMG performance is even three orders of magnitude higher than those of other reported TMGs, such as the passive TMG using Gd (maximum P_d = 1.1 mW/m^3 K and average $P_d = 3.1 \times 10^{-3}$ mW/m^3 K) [28], the active TMG using $Ni_{45}Co_5Mn_{40}Sn_{10}$ bulk (maximum $P_d = 5 \times 10^{-3}$ mW/m^3 K) [22], and the active TMG using Gd sheet (maximum P_d = 0.16 mW/m^3 K) [32].

5. Conclusions

In conclusion, an active TMG using Gd metal has been successfully built to convert the low-grade waste heat into electrical energy. Positive and negative currents *I* are induced alternatively by the TMG due to the reversible thermal-induced FM-PM magnetic transition. The *dT/dt* around *TC* during the heating is larger than the one during the cooling, thus leading to the higher *I* during the heating according to $I \propto (dB/dT)(dT/dt)$. Furthermore, the influences of different key device and material parameters on the TMG performance are investigated systematically by the finite element simulation. It demonstrates that the TMG performance is influenced largely by both device and material parameters, especially

Table 2
The comparison of key device parameters before and after optimization.

	Non-optimization	Optimization
Sample cabin size	145 mm	20 mm
System temperature range	288 ~ 353 K	276 ~ 361 K
Cycle period	60 s	10 s

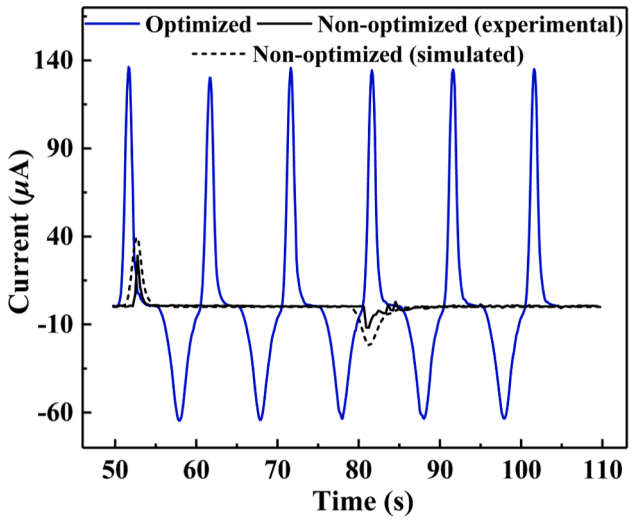

Fig. 13. Comparison of the experimental and simulated *I-t* before optimization and the simulated *I-t* after optimization.

the cabin size and C_P. Based on that, we optimized the key device parameters in the simulation, i.e., the sample cabin size is shortened from 145 mm to 20 mm, the system temperature range is expanded from 288 ~ 353 K to 276 ~ 361 K, and the cycle period is reduced from 60 s to 10 s. In comparison with the non-optimized experimental peak *I* of 28.8 μA, the simulated peak *I* increases largely to 136.1 μA after the optimization. Moreover, the maximum P_d and average P_d increase by one order of magnitude from 0.16 mW/m^3 K and 0.01 mW/m^3 K to 3.6 mW/m^3 K and 0.4 mW/m^3 K, respectively. This improved TMG performance is also much higher than those of other reported TMGs. Consequently, this work provides a feasible way to improve the TMG performance efficiently, which would greatly promote the application of TMG technology for the low-grade waste heat recovery.

CRediT authorship contribution statement

Xianliang Liu: Methodology, Software, Investigation, Data curation, Writing – original draft. **Hu Zhang:** Conceptualization, Supervision, Formal analysis, Resources, Funding acquisition, Writing – review & editing. **Haodong Chen:** Methodology, Validation. **Zhihui Ma:** Methodology, Investigation. **Kaiming Qiao:** Validation, Formal analysis. **Longlong Xie:** Visualization. **Zhiqiang Ou:** Formal analysis. **Jing Wang:** Software, Resources. **Fengxia Hu:** Software, Resources. **Baogen Shen:** Software, Resources, Funding acquisition.

Declaration of Competing Interest

The authors declare that they have no known competing financial interests or personal relationships that could have appeared to influence the work reported in this paper.

Data availability

Data will be made available on request.

Acknowledgements

This work was supported by the National Natural Science Foundation of China (Grant Nos.: 52171169, 52101210, 52088101); the National Key Research and Development Program of China (Grant Nos.: 2021YFB3501204, 2020YFA0711502); the China Postdoctoral Science Foundation (Grant No.: 2021M690346); the Fundamental Research Funds for the Central Universities and the Youth Teacher International Exchange & Growth Program (Grant No.: QNXM20210014).

References

[1] C. Forman, I.K. Muritala, R. Pardemann, B. Meyer, Estimating the global waste heat potential, Renew. Sust. Energ. Rev. 57 (2016) 1568–1579.
[2] H.Y. Lu, L. Price, Q. Zhang, Capturing the invisible resource: analysis of waste heat potential in Chinese industry, Appl. Energy 161 (2016) 497–511.
[3] R.A. Kishore, S. Priya, A review on low-grade thermal energy harvesting: materials, methods and devices, Materials 11 (8) (2018) 1433.
[4] C. Haddad, C. Périlhon, A. Danlos, M.X. François, G. Descombes, Some efficient solutions to recover low and medium waste heat: competitiveness of the thermoacoustic technology, Energy Procedia 50 (2014) 1056–1069.
[5] Z.Y. Xu, R.Z. Wang, C. Yang, Perspectives for low-temperature waste heat recovery, Energy 176 (2019) 1037–1043.
[6] P. Aranguren, M. Araiz, D. Astrain, A. Martínez, Thermoelectric generators for waste heat harvesting: a computational and experimental approach, Energ. Convers Manage. 148 (2017) 680–691.
[7] W. He, R. Guo, S.C. Liu, K. Zhu, S.X. Wang, Temperature gradient characteristics and effect on optimal thermoelectric performance in exhaust power-generation systems, Appl. Energy 261 (2020), 114366.
[8] S. Lan, A. Smith, R. Stobart, R. Chen, Feasibility study on a vehicular thermoelectric generator for both waste heat recovery and engine oil warm-up, Appl. Energy 242 (2019) 273–284.
[9] S. Liu, B.K. Hu, D.W. Liu, F. Li, J.F. Li, B. Li, L.L. Li, Y.H. Lin, C.W. Nan, Micro-thermoelectric generators based on through glass pillars with high output voltage enabled by large temperature difference, Appl. Energy 225 (2018) 600–610.
[10] C.R. Bowen, J. Taylor, E. LeBoulbar, D. Zabek, A. Chauhan, R. Vaish, Pyroelectric materials and devices for energy harvesting applications, Energy Environ. Sci. 7 (12) (2014) 3836–3856.
[11] H. Nguyen, A. Navid, L. Pilon, Pyroelectric energy converter using co-polymer P (VDF-TrFE) and Olsen cycle for waste heat energy harvesting, Appl. Therm. Eng. 30 (14–15) (2010) 2127–2137.
[12] Y. Yang, W.X. Guo, K.C. Pradel, G. Zhu, Y.S. Zhou, Y. Zhang, Y.F. Hu, L. Lin, Z. L. Wang, Pyroelectric nanogenerators for harvesting thermoelectric energy, Nano Lett. 12 (6) (2012) 2833–2838.
[13] K. Wang, J. Zhang, N. Zhang, D.M. Sun, K. Luo, J. Zou, L.M. Qiu, Acoustic matching of a traveling-wave thermoacoustic electric generator, Appl. Therm. Eng. 102 (2016) 272–282.
[14] R. Yang, A. Meir, G.Z. Ramon, Theoretical performance characteristics of a travelling-wave phase-change thermoacoustic engine for low-grade heat recovery, Appl. Energy 261 (2020), 114377.
[15] Z.B. Yu, A.J. Jaworski, S. Backhaus, Travelling-wave thermoacoustic electricity generator using an ultra-compliant alternator for utilization of low-grade thermal energy, Appl. Energy 99 (2012) 135–145.
[16] T. Christiaanse, E. Brück, Proof-of-concept static thermomagnetic generator experimental device, Metall. Mater. Trans. E. 1 (1) (2014) 36–40.
[17] K. Deepak, M.S. Pattanaik, R.V. Ramanujan, Figure of merit and improved performance of a hybrid thermomagnetic oscillator, Appl. Energy 256 (2019), 113917.
[18] K. Deepak, V.B. Varma, G. Prasanna, R.V. Ramanujan, Hybrid thermomagnetic oscillator for cooling and direct waste heat conversion to electricity, Appl. Energy 233–234 (2019) 312–320.
[19] M. Gueltig, H. Ossmer, M. Ohtsuka, H. Miki, K. Tsuchiya, T. Takagi, M. Kohl, High frequency thermal energy harvesting using magnetic shape memory films, Adv. Energy Mater. 4 (17) (2014) 1400751.
[20] M. Gueltig, F. Wendler, H. Ossmer, M. Ohtsuka, H. Miki, T. Takagi, M. Kohl, High-performance thermomagnetic generators based on heusler alloy films, Adv. Energy Mater. 7 (5) (2017) 1601879.
[21] R.A. Kishore, D. Singh, R. Sriramdas, A.J. Garcia, M. Sanghadasa, S. Priya, Linear thermomagnetic energy harvester for low-grade thermal energy harvesting, J. Appl. Phys. 127 (4) (2020), 044501.
[22] V. Srivastava, Y.T. Song, K. Bhatti, R.D. James, The direct conversion of heat to electricity using multiferroic alloys, Adv. Energy Mater. 1 (1) (2011) 97–104.
[23] A. Waske, D. Dzekan, K. Sellschopp, D. Berger, A. Stork, K. Nielsch, S. Fähler, Energy harvesting near room temperature using a thermomagnetic generator with a pretzel-like magnetic flux topology, Nat. Energy 4 (1) (2019) 68–74.
[24] X. Niu, J.L. Yu, S.Z. Wang, Experimental study on low-temperature waste heat thermoelectric generator, J. Power Sources 188 (2) (2009) 621–626.
[25] S. Pandya, J. Wilbur, J. Kim, R. Gao, A. Dasgupta, C. Dames, L.W. Martin, Pyroelectric energy conversion with large energy and power density in relaxor ferroelectric thin films, Nat. Mater. 17 (5) (2018) 432–440.
[26] D. Vuarnoz, A. Kitanovski, C. Gonin, Y. Borgeaud, M. Delessert, M. Meinen, P. W. Egolf, Quantitative feasibility study of magnetocaloric energy conversion utilizing industrial waste heat, Appl. Energy 100 (2012) 229–237.
[27] R.A. Kishore, S. Priya, A review on design and performance of thermomagnetic devices, Renew. Sust. Energ. Rev. 81 (2018) 33–44.
[28] C.C. Chen, T.K. Chung, C.Y. Tseng, C.F. Hung, P.C. Yeh, C.C. Cheng, A miniature magnetic-piezoelectric thermal energy harvester, IEEE Trans. Magn. 51 (7) (2015) 1–9.
[29] H.C. Song, D. Maurya, J. Chun, Y. Zhou, M.E. Song, D. Gray, N.K. Yamoah, D. Kumar, A. McDannald, M. Jain, Modulated magneto-thermal response of $La_{0.85}Sr_{0.15}MnO_3$ and $(Ni_{0.6}Cu_{0.2}Zn_{0.2})Fe_2O_4$ composites for thermal energy harvesters, Energy Harvest Syst. 4 (2017) 57–65.

[30] C. Rodrigues, A. Pires, I. Gonçalves, D. Silva, J. Oliveira, A. Pereira, J. Ventura, Hybridizing triboelectric and thermomagnetic effects: a novel low-grade thermal energy harvesting technology, Adv. Funct. Mater. 32(21) (2022) 2110288.
[31] J.F. Elliott, Thermomagnetic generator, J. Appl. Phys. 30 (11) (1959) 1774–1777.
[32] C. Jiang, S.M. Zhu, G.Y. Yu, E.C. Luo, K. Li, Numerical and experimental investigations on a regenerative static thermomagnetic generator for low-grade thermal energy recovery, Appl. Energy 311 (2022) 17.
[33] Z.H. Ma, H.D. Chen, X.L. Liu, C.F. Xing, M.L. Wu, Y.X. Wang, P.R. Liu, Z.Q. Ou, J. Shen, S.V. Taskaev, K.W. Long, Y. Long, H. Zhang, Thermomagnetic generation performance of Gd and La(Fe, Si)$_{13}$H$_y$/In material for low-grade waste heat recovery, Adv. Sustain Syst. 5 (2021) 2000234.
[34] D. Solomon, Improving the performance of a thermomagnetic generator by cycling the magnetic field, J. Appl. Phys. 63 (3) (1988) 915–921.
[35] R.A. Kishore, B. Davis, J. Greathouse, A. Hannon, D.E. Kennedy, A. Millar, D. Mittel, A. Nozariasbmarz, M.G. Kang, H.B. Kang, M. Sanghadasa, S. Priya, Energy scavenging from ultra-low temperature gradients, Energy Environ. Sci. 12 (3) (2019) 1008–1018.
[36] A. Homadi, T. Hall, L. Whitman, Study a novel hybrid system for cooling solar panels and generate power, Appl. Therm. Eng. 179 (2020) 1–8.
[37] R. Zeeshan, M.U. Ahmed, Y. Mehmood, J. Kim, W. Lee, Chun, Harnessing low-grade waste heat by operating a hybrid piezoelectric-electromagnetic energy harvester combined with a thermomagnetic engine, Int. J. Energy Res. 44 (13) (2020) 10710–10723.
[38] B.R. Hansen, L.T. Kuhn, C.R.H. Bahl, M. Lundberg, C. Ancona-Torres, M. Katter, Properties of magnetocaloric La(Fe Co, Si)13 produced by powder metallurgy, J. Magn. Magn. Mater. 322 (21) (2010) 3447–3454.
[39] Y.X. Wang, H. Zhang, E.K. Liu, X.C. Zhong, K. Tao, M.L. Wu, C.F. Xing, Y.N. Xiao, J. Liu, Y. Long, Outstanding comprehensive performance of La(Fe, Si)$_{13}$H$_y$/In composite with durable service life for magnetic refrigeration, Adv. Electron Mater. 4 (5) (2018) 1700636.
[40] Y.Y. Ou, M.X. Zhang, A. Yan, W. Wang, F. Guilloud, J. Liu, Plastically deformed La-Fe-Si: Microstructural evolution, magnetocaloric effect and anisotropic thermal conductivity, Acta Mater. 187 (2020) 1–11.
[41] A.B. Batdalov, A.M. Aliev, L.N. Khanov, V.D. Buchel'nikov, V.V. Sokolovskiy, V. V. Koledov, V.G. Shavrov, A.V. Mashirov, E.T. Dil'mieva, Magnetic, thermal, and electrical properties of an Ni$_{45.37}$Mn$_{40.91}$In$_{13.72}$ Heusler alloy, J. Exp. Theor. Phys. 122 (5) (2016) 874–882.
[42] Y.H. Qu, D.Y. Cong, X.M. Sun, Z.H. Nie, W.Y. Gui, R.G. Li, Y. Ren, Y.D. Wang, Giant and reversible room-temperature magnetocaloric effect in Ti-doped Ni-Co-Mn-Sn magnetic shape memory alloys, Acta Mater. 134 (2017) 236–248.
[43] K. Fukamichi, A. Fujita, S. Fujieda, Large magnetocaloric effects and thermal transport properties of La(FeSi)$_{13}$ and their hydrides, J. Alloys Compd. 408 (2006) 307–312.
[44] S. Fujieda, Y. Hasegawa, A. Fujita, K. Fukamichi, Thermal transport properties of magnetic refrigerants La(Fe$_x$Si$_{1-x}$)$_{13}$ and their hydrides, and Gd$_5$Si$_2$Ge$_2$ and MnAs, J. Appl. Phys. 95 (5) (2004) 2429–2431.